frontiers in Energy Research

ORIGINAL RESEARCH
published: 29 March 2019
doi: 10.3389/fenrg.2019.00034

Use of Ni Catalysts Supported on Biomorphic Carbon Derived From Lignocellulosic Biomass Residues in the Decomposition of Methane

*Manuel Azuara, Nieves Latorre, José I. Villacampa, Victor Sebastian, Fernando Cazaña, Eva Romeo and Antonio Monzón**

Instituto de Nanociencia de Aragón, Instituto de Ciencia de Materiales de Aragón, University of Zaragoza, Zaragoza, Spain

In this work, we present the results of production of carbonaceous nanomaterials by decomposition of methane on a catalyst of Ni supported on a Biomorphic Carbon. The catalyst was prepared by thermal decomposition in a reductive atmosphere of vine shoots previously impregnated with the Ni precursor. In order to optimize the reaction productivity and selectivity, the effect of the main operational conditions (reaction temperature and feed composition) has been studied in a thermobalance. The main textural properties, BET area of 63 m^2/g and 56% of microporosity, of the catalyst synthesized indicates that these materials are suitable for gas-phase reactions even in harsh conditions. Thus, the catalyst has proved to be active in the synthesis of carbon nanofibers and graphene related materials at elevated temperatures. The productivity, type, and quality of the carbonaceous nanomaterials obtained are deeply dependent on the operating conditions during the reaction. As an important fact, is has been obtained that the reaction temperature strongly affects the type of the nanomaterial produced. Thus, it is produced CNFs of bamboo type at temperatures until 850°C. Above this critical temperature, it is mainly obtained nanolayers of graphitic nature. The characterization results indicate that the highest quality graphenic materials were obtained operating at 950°C with 14.3% of CH_4 and 14.3% of H_2. The kinetic model used to analyze the experimental data is based on the more relevant stages of the mechanism of reaction.

Keywords: lignocellulose, residue, biomorphic carbon, Ni, methane decomposition, hydrogen

OPEN ACCESS

Edited by:
Fernando Bimbela, Universidad Pública de Navarra, Spain

Reviewed by:
Jose Luis Pinilla, Instituto de Carboquímica (ICB), Spain
Ahmet Arisoy, Istanbul Technical University, Turkey
Jude Azubuike Onwudili, Aston University, United Kingdom

****Correspondence:***
Antonio Monzón
amonzon@unizar.es

Specialty section:
This article was submitted to Advanced Fossil Fuel Technologies, a section of the journal Frontiers in Energy Research

Received: *16 December 2018*
Accepted: *11 March 2019*
Published: *29 March 2019*

Citation:
Azuara M, Latorre N, Villacampa JI, Sebastian V, Cazaña F, Romeo E and Monzón A (2019) Use of Ni Catalysts Supported on Biomorphic Carbon Derived From Lignocellulosic Biomass Residues in the Decomposition of Methane. Front. Energy Res. 7:34. doi: 10.3389/fenrg.2019.00034

INTRODUCTION

The large number of applications found in recent decades for Carbonaceous Nanomaterials (CNMs), like carbon nanotubes, grapheme, and Graphene Related Materials (GRMs) like the so-called Few Layer Graphene (FLG), has led to develop numerous studies to know, develop and apply the excellent properties of these materials (Ji et al., 2011; Li et al., 2011; Novoselov, 2011; Siamaki et al., 2011; Cheng et al., 2012; Hu et al., 2014; Nine et al., 2015; Shin and Kim, 2015).

The catalytic decomposition of hydrocarbons in vapor phase (CCVD) is one of the most important alternative production methods of these nanomaterials. This process shows several advantages such as easily scalability and cheaper production (Baddour and Briens, 2005). If the carbon source used is methane, it is obtained as an additional advantage, the co-production of

pure hydrogen (Ahmed et al., 2009; Amin et al., 2011; Li et al., 2011). The obtained Hydrogen can be used as reactive in chemical processes, like hydrogenation or desulphurization, or used as fuel, contributing to the decrease in the use of polluting fossil fuels (Zhang et al., 2018). Furthermore, the hydrogen produced in this process is totally free of CO and CO_2 and can be directly used in fuel cells. The absence of CO prevents the electro-catalyst poisoning (Ashik et al., 2015).

On the other hand, the growing concern for the environment and the need to protect it, is leading to the investigation of new processes to obtain high added value products from renewable natural sources (El Achaby et al., 2018). In this context, one of the natural sources that can be used with more success is lignocellulosic materials. One of the possible sources to obtain lignocellulosic materials may be agricultural wastes, such as vine shoots, which are generated in the pruning and constitute an important waste for wine industry. For example, taking Spanish data, it can be considered the production of $1.9{\cdot}10^6$ tons of vine shoots per year, considering about 1,000 kha used for vine cultivation in the country in 2016 and assuming a waste yield of 1.9 ton/ha (dry basis) (Manyà et al., 2018). These shoots are often shredded and deposited on the soil to return the organic matter. However, this treatment can cause damage to the health of the vineyards due to the potential risk of increased inoculum (Duca et al., 2016; Azuara et al., 2017).

The process based in the decomposition of lignocellulosic materials using a reducing or inert atmosphere at high temperatures and high heating rates is called biomorphic mineralization and allows converting structures formed by a biological process, e.g., wood and lignocellulosic biomass to inorganic materials with different potential applications (Mann, 2001; Will et al., 2010). Furthermore, if the materials are previously impregnated with metallic catalytic precursors, a catalyst is obtained in a single step. The catalyst is formed by the metallic nanoparticles dispersed on the biomorphic carbonaceous support (BC) (Fan et al., 2009). The possibility of using different metals and lignocellulosic raw materials makes the method a versatile tool to synthesize catalysts of different compositions and metal contents (Cazaña et al., 2015, 2018a).

The potential use of these carbonaceous materials obtained from lignocellulosic residue, e.g., vine shoot, as support of catalysts in different reactions of energy and/or environmental importance is of great interest, for example, in the above commented methane decomposition reaction to the simultaneous production of pure H_2, free of CO and CO_2, and of carbonaceous nanomaterials (CNMs).

In the present work, we study the kinetics of production of carbonaceous nanomaterials by decomposition of methane on a catalyst of Ni supported on a Biomorphic Carbon obtained by thermal decomposition of vine shoots. The influence of reaction temperature and feed composition on the quantity and the kind of CNMs obtained has been studied.

Finally, a key factor for the control in the selectivity of the CCVD process toward the type of carbonaceous nanomaterial desired is to know the reaction mechanism. The use of a kinetic model to analyse the CDM reaction data, based on the main stages of the mechanisms and which also consider the catalyst deactivation allows us optimizing the process (Villacampa et al., 2003; Pérez-Cabero et al., 2004; Chen et al., 2005; Dussault et al., 2007; Monzón et al., 2008; Benito et al., 2009; Martínez-Hansen et al., 2009; Latorre et al., 2010a, 2011; Romeo et al., 2014).

MATERIALS AND METHODS

Materials

The vine shoots used in this work were supplied by a winery from the Denomination of Origin Somontano (Huesca, Spain). The material was prepared (milling and sieving) to obtain a homogeneous particle size distribution between 0.250 and 1.18 mm. The metal precursor used was Ni (II) Nitrate 6-hydrate supplied by Panreac Quimica SAU (ref.: 14144.1209).

Catalyst Preparation

The synthesis of the catalyst was carried out following different steps: First, the vine shoots were dried at 100°C overnight. Then, they were impregnated by incipient wetness with the Ni aqueous solution. After impregnation, the solid was dried at 80°C overnight. Finally, thermal decomposition was carried out. During this decomposition, Ni nanoparticles are generated, which catalyze partly the gasification of the carbonaceous support, generating greater porosity, BET area, and definitely better textural properties of the final catalyst. The main variables of this step are: atmosphere composition during de thermal treatment, temperature, duration time and heat rate to reach the final temperature (Cazaña et al., 2015, 2018a,b). In this case, thermal decomposition was carried out in reducing atmosphere (50% H_2, 50% N_2) at 800°C for 180 min. The heating rate used to reach the decomposition temperature was ∼40°C/min. Finally, the catalyst was cooled under N_2 atmosphere for 2 h.

Catalyst and Carbonaceous Nanomaterials Characterization

In order to know the type of carbon nanomaterials formed in the reaction and the textural and structural properties of the catalyst, different characterization techniques were used. A Mettler Toledo TGA/SDTA 851 analyzer, using 50 mL/min, was used to carry out thermogravimetric analyses in air (TGA-Air). This technique allows calculating the final percentage of Ni on the biomorphic carbon support obtained after the thermal decomposition of the vine shoots, knowing the impregnated initial amount of Ni and the final composition of the solid residue after the combustion in the TGA-Air experiment (NiO and ashes). Nitrogen adsorption–desorption isotherms at 77 K were developed to know the specific area and porosity of the catalyst. The equipment used was a TriStar 3000 instrument (Micromeritics Instrument Corp.). BET specific surface areas were measured from the adsorption branches in the relative pressure range of 0.01–0.10. The micropore volume estimation was made by means of the Dubinin-Radushkevich method (Dubinin and Radushkevich, 1947). The X-ray diffraction (XRD) patterns were recorded within the range of 5–90° (2θ) with a Rigaku D/Max 2500 apparatus operated at 3.2 kW (40 kV, 80 mA) and with a rotatory anode of Cu using Cu Kα radiation. A FEI Tecnai T-20 microscope, operated at 200 kV, was used to obtain

Transmission electron microscopy (TEM) images. Scanning electron microscopy (SEM) micrograph images were realized in a FEI Inspect F50 microscope, operated at 10 kV. Raman spectroscopy was used to know the carbonaceous characteristics of the catalyst support and of the materials formed during the reaction. The equipment uses a WiTec Alpha300 Confocal Raman Microscope, with a 532 nm laser excitation beam.

Catalytic Decomposition of Methane (CDM)

The CDM reaction was carried out at atmospheric pressure in a thermobalance (CI Electronics Ltd., UK, model MK2) operated as a continuous differential fixed-bed reactor (i.e., low reactant conversions, <10% methane conversion). Under these conditions a direct measurement of the reaction rate and therefore, of the catalyst activity is obtained. This experimental system allows continuous recording of the variations of sample weight and temperature during reaction. The reaction conditions were: sample weight: 25 mg; total flow-rate: 700 NmL/min.; temperature: 700–950°C; feed composition: $\%CH_4$: from 4.3 to 57.1%, 14.3% of H_2 and N_2 as balance. Blank experiments without catalyst are carried out to check the possible formation of carbonaceous deposits from the gas phase decomposition of methane, not observing the deposition of carbon in any case.

KINETICS AND MECHANISM OF CARBONACEOUS NANOMATERIALS GROWTH

In order to describe the kinetics of carbonaceous material formation by catalytic methane decomposition, we have adapted a phenomenological model previously developed by our group (Rodríguez et al., 1995; Monzón et al., 2003, 2008; Latorre et al., 2010a). This model considers the more relevant steps of the reaction mechanism that can be summarized in the following steps: (i) adsorption and cracking of methane molecules on the Ni nanoparticles; (ii) reaction of the adsorbed carbon atoms with the surface of the Ni nanoparticles, forming a metastable Ni carbide which, at the reaction conditions, decomposes introducing the carbon atoms at the metallic subsurface; (iii) diffusion and precipitation of carbon atoms forming, depending on the experimental conditions used, different types of nanomaterials like carbon nanotubes, carbon nanofibers, or graphitic nanolayers covering the metallic nanoparticles; (iv) eventually, partial exfoliation of the graphenic layers due to the action of the atmosphere of reaction, mainly hydrogen. After this step, at high temperature of reaction it can be observed the formation of separate sheets of graphene and FLG (see section Results and discussion). **Figure 1** shows a scheme of the main features of the above mechanism of formation of carbonaceous nanomaterials over the catalyst nanoparticles.

On the other side, given that the methane conversions attained at the reactor exit are very low (<10%), it is not necessary to consider the equilibrium reaction in the rate expression.

Regarding to the catalytic sites involved in the reaction, although the carbonaceous materials has been also used in the methane decomposition (Suelves et al., 2008; Serrano et al., 2013), its intrinsic activity is quite less than that of Ni. In consequence, it has not been included in the model, in order to not increase the number of kinetic parameters to calculate.

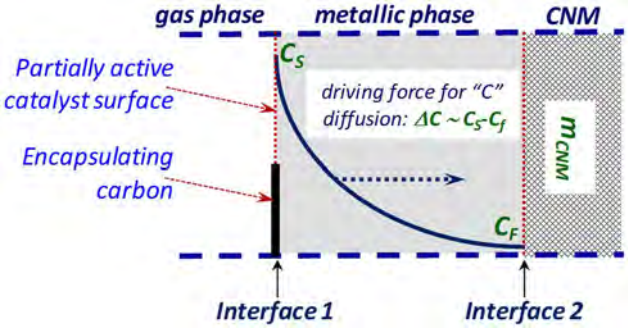

FIGURE 1 | Scheme of the mechanism of formation of carbonaceous nanomaterials by catalytic decomposition of hydrocarbons.

In addition to all these phenomena, it must be considered the deactivation of the catalyst. The decay of the catalyst activity is consequence of several factors like coke fouling of the external Ni surface, the falling of the methane diffusion rate through the nanolayers of graphite, the reconstruction of the Ni nanoparticles during the reaction, and the steric hindrance for the growth of CNTs, CNFs (Monzón et al., 2008; Latorre et al., 2010a). Finally, the catalyst shows residual activity. The presence of this residual activity is due to the effect of H_2 generated *in situ* during the reaction, which gasifies part of the carbon formed on the surface of the Ni, cleaning a fraction of the active centers, which are responsible for this stationary activity.

In spite of all (Monzón et al., 2008; Latorre et al., 2010a; Cazaña et al., 2018a), the use of simplified models that nevertheless are able to capture the main part of the influence of the main variable of operation, i.e., methane concentration and reaction temperature could be very useful to rationalize the process of production of these materials.

Kinetic Modeling of Carbon Growth

The methane decomposition rate can be measured directly from the rate of carbon formation over the catalyst $(r_C)_t$. According to the mechanism of reaction, the rate of carbon growth is determined by the net rate of diffusion of carbon atoms, which is driven by the difference of concentration of carbon at gas-side surface of the Ni nanoparticles, C_S, and at the rear part of the nanoparticles, initially in contact with the support, C_F. This part, is in fact the exit site for the segregation of the carbonaceous nanomaterials. It can be assumed that C_F, is very low in comparison with C_S, therefore, the reaction rate is given by:

$$(r_C)_t = \left(\frac{dm_C}{dt}\right)_t = k_C \cdot (C_S - C_F) \cdot a(t) \cong k_C \cdot C_S \cdot a(t) = k_C \cdot C_{S_m} \cdot \theta_S \cdot a(t) \quad (1)$$

The term k_C is the effective coefficient of carbon transport, has units of time^{-1}, and depends on the average size of the

metallic crystallites, the metallic exposed area, and the carbon atom diffusivity on the metallic nanoparticles. In addition, and taking into account the possible effect of catalyst deactivation, catalyst activity, a, is also included in the expression.

In turn, the value of the C_S can be calculated as a function of the degree of carburization of the Ni surface, θ_S, as follows: $\theta_S = C_S/C_{S_m}$, where the term C_{Sm} is the concentration of carbon at the gas-side of the Ni nanoparticles at complete carburization. Assuming that the carburization can be described (Latorre et al., 2010a) as a first order process, the evolution of the carburization process with time is given by:

$$r_S = \frac{d\theta_S}{dt} = \psi_S \cdot (1 - \theta_S) \leftrightarrow \theta_S = 1 - \exp(-\psi_S \cdot t) \quad (2)$$

On the other side, the results shown in **Figures 6**, **9**, indicate the existence of a remaining value of the reaction rate, we have used the so-called "Deactivation model with Residual Activity," (Monzón et al., 2003) to model the evolution of catalyst activity with time. In this case, the net deactivation rate is given by:

$$\begin{aligned} -\frac{da}{dt} &= \psi_d \cdot a - \psi_r \cdot (1 - a) \\ &\rightarrow \quad a(t) = a_R + (1 - a_R) \cdot \exp(-\psi_G \cdot t) \\ \psi_G &= \psi_d + \psi_r; \quad a_R = \frac{\psi_r}{\psi_d + \psi_r} = \frac{\psi_r}{\psi_G} \end{aligned} \quad (3)$$

The terms ψ_d and ψ_r have dimensions of time^{-1} and are kinetic parameters of deactivation and regeneration, respectively. For a given catalyst composition and activation procedure, both depend on the experimental conditions, mainly temperature, and feed composition, used during the reaction. The term a_R corresponds to the residual activity of the catalysts, which will be zero for the case of irreversible deactivation. After combination of Equations (1–3), the rate of carbon formation is given by:

$$\begin{aligned} \frac{dm_C}{dt} &= j_{C_0} \cdot \theta_S(t) \cdot a(t) \\ &= j_{C_0} \cdot (1 - \exp(-\psi_S \cdot t)) \cdot (a_R + (1 - a_R) \cdot \exp(-\psi_G \cdot t)) \\ j_{C_0} &= k_C \cdot C_{S_m} \end{aligned} \quad (4)$$

The term m_C is the amount of carbon accumulated over the catalysts, expressed as g_C/g_{cat}. The parameter j_{C0} represents the intrinsic carbon growth rate for the fresh catalyst, measured in gC/gcat·min, and depends on the effective carbon diffusivity in the Ni nanoparticles at the operating conditions. The term C_{Sm} depends on the carbon solubility which determines the driving force for the diffusion of the carbon atoms through the metallic nanoparticles (Latorre et al., 2010a,b). Finally, after integration of Equation (4), the evolution of carbon content along time can be expressed as:

$$\begin{aligned} m_C &= j_{C_0} \cdot \left(a_R \cdot \left(t - \frac{1 - \exp(-\psi_S \cdot t)}{\psi_S} \right) \right. \\ &\quad \left. + (1 - a_R) \cdot \left(\frac{1 - \exp(-\psi_G \cdot t)}{\psi_G} - \frac{1 - \exp(-\psi_{SG} \cdot t)}{\psi_{SG}} \right) \right) \\ \psi_{SG} &= \psi_S + \psi_G \end{aligned} \quad (5)$$

For the particular case of very rapid carburization step, i.e., $\Psi_S \rightarrow \infty$, it can be assumed that $\theta_S = 1$ from the beginning, and consequently the above equations are simplified to:

$$\begin{aligned} (r_C)_t &= j_{C_0} \cdot \left(a_R + (1 - a_R) \cdot \exp(-\psi_G \cdot t) \right) \rightarrow \\ \rightarrow m_C &= j_{C_0} \cdot \left(a_R \cdot t + \frac{(1 - a_R)}{\psi_G} \cdot \left(1 - \exp(-\psi_G \cdot t) \right) \right) \end{aligned} \quad (6)$$

In addition to the above considerations, it must be taken into account that there is a change of the type of carbonaceous nanomaterial formed depending of the reaction temperature, see **Figure 8**. Thus, at temperatures below 900°C, the nanomaterials formed are mainly carbon nanotubes and hollow nanofibers, see **Figures 8A,B** (Villacampa et al., 2003; Dussault et al., 2007). However, above this temperature, the carbon grown is mainly composed by nanoplatelets of graphite surrounding the metallic nanoparticles, avoiding the formation of CNFs. Apparently, at this critical temperature there is a change in the balance between the nucleation and precipitation steps of the reaction mechanism. Below 900°C, is predominant the precipitation step, characterized by the presence of few points of nucleation, and therefore favoring the growth of CNFs.

Nevertheless, at higher reaction temperatures, numerous nucleation points at the surface of the metallic nanoparticles are generated, creating many points for the exit of the dissolved carbon, which eventually leads to the formation of the graphenic materials surrounding the metallic nanoparticles observed at these conditions (see **Figures 8C–F**) (Cazaña et al., 2018a).

In order to include this fact in the model, we have incorporated an additional parameter in the Equation 6 that allows modulating the effect of the diffusion time of carbon in each range of reaction temperature. This additional parameter, n, is introduced as a power-law function of the reaction time, and the final expression used for the fitting the experimental data is:

$$m_C = j_{C_0} \cdot \left(a_R \cdot t^n + \frac{(1 - a_R)}{\psi_G} \cdot \left(1 - \exp(-\psi_G \cdot t^n) \right) \right) \quad (7)$$

In summary, the evolution of the carbon concentration is calculated as a function of the following parameters: j_{C0}, ψ_d, ψ_r, and n, which are dependent on the temperature and gas composition used in each experiment. The dependence with respect to the methane concentration is expressed as power-law functions:

$$\begin{aligned} j_{C_0} &= k_C \cdot p_{CH_4}^{m_C} \\ \psi_d &= k_d \cdot p_{CH_4}^{m_d} \\ \psi_r &= k_r \cdot p_{CH_4}^{m_r} \end{aligned} \quad (8)$$

The values of k_C, k_d, and k_r in the above equations follow an Arrhenius-type dependence with the temperature:

$$\begin{aligned} k_C &= k_{C_0} \cdot \exp(-E_C/RT) \\ k_d &= k_{d_0} \cdot \exp(-E_d/RT) \\ k_r &= k_{r_0} \cdot \exp(-E_r/RT) \end{aligned} \quad (9)$$

Where E_C, E_d, and E_r represent the apparent activation energies for each parameter, and k_{C0}, k_{d0}, and k_{r0} are the corresponding pre-exponential factors. The parameters have been estimated by non-linear least-squares multivariable regression. The maximized objective function was the *Model Selection Criterion* (MSC) defined as Sclove (1987) and Ward (2008):

$$MSC = \ln\left(\frac{SST}{SSR}\right) - \left(\frac{2p}{n_p - p}\right) \tag{10}$$

In this expression, p represents the number of parameters and n_p the number of experimental points. The terms SST and SSR are the sum of total squares and the sum of the squared residuals, respectively. These terms are defined as:

$$SST = \sum_{i=1}^{i=n_p} \left(m_C^{\exp} - \overline{m_C^{\exp}}\right)^2$$
$$SSR = \sum_{i=1}^{i=n_p} \left(m_C^{\exp} - m_C^{cal}\right)^2 \tag{11}$$

One key advantage of the use of the MSC, unlike the SSR, is that it allows a rigorous statistical discrimination among several models with different number of parameters (Ward, 2008; Armenise et al., 2013).

RESULTS AND DISCUSSION

Catalyst Characterization

Figure 2 shows the TGA-air curves for the biomorphic carbon prepared from wine shoots and for the Ni/BC catalyst. The amount of remaining material after oxidation corresponds to ashes in the case of the biomorphic carbon and to NiO and ashes for the Ni/BC catalyst. The final composition of the catalyst, obtained from these results, is 24% of Ni (wt.%) with respect to the biomorphic carbon formed. The catalyst was synthesized with a nominal content of 3.5%wt of Ni respect to the initial amount of shoot. After the preparation, the final amount of metal was quite higher (24% wt.), as expected due to the loss of an important part of the raw material mass during their thermal decomposition.

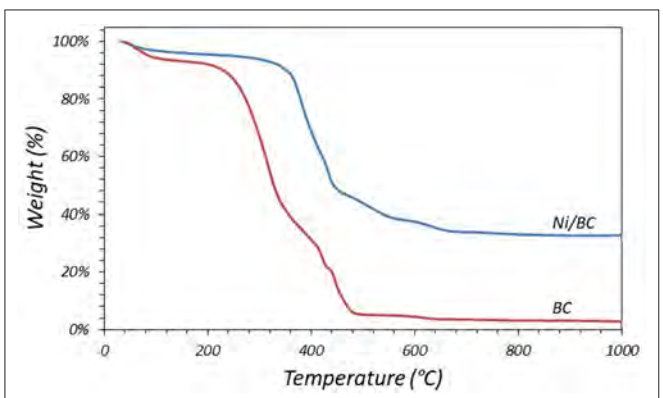

FIGURE 2 | TGA-Air analyses for biomorphic carbon and Ni/BC catalyst.

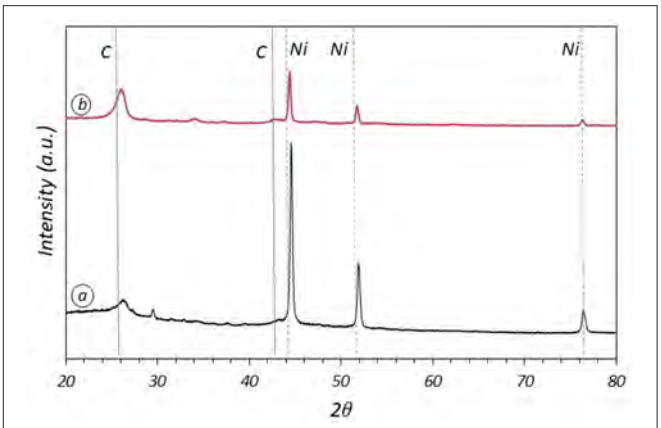

FIGURE 3 | XRD pattern of fresh catalyst **(a)** and after reaction at 950°C **(b)**.

The textural characteristics were studied by N_2 adsorption. The results for the Ni/BC catalyst give BET surface area of 63 m^2/g a pore volume of 0.125 cm^3/g with a percentage of micropore volume of 56%. For the biomorphic carbon obtained without previous impregnation with the Ni precursor, the results are 17 m^2/g for the BET area, and 0.013 cm^3/g of pore volume, with a 42% of micropores. Therefore, in this case, the addition of Ni enhances the development of the structure of the carbonaceous support, increasing both the area and the pore volume of the support.

The XRD patterns of the fresh catalyst and after reaction at 950°C can be observed in **Figure 3**. In both cases, the peaks corresponding to metallic Ni can be observed and there are not peaks associated to NiO. According to Scherrer equation the average Ni particle sizes are 35 and 31 nm, respectively. These results corroborate that the high decomposition temperature used during the synthesis of the catalyst, 800°C, minimizes the subsequent sintering during the reaction. The apparent redispersion of the Ni nanoparticles after reaction can be a consequence of a change in the size distribution during the formation of the carbonaceous nanomaterials at the higher temperatures.

The peak obtained at 26 and 43°Corresponds to the plane (002) and (100), respectively, of the carbon formed after the decomposition step at 800°C, indicating that part of the biomorphic material formed during the preparation of the catalyst has an incipient graphitic structure. After reaction, these peaks mainly correspond with the accumulation of graphitic/graphenic material over the surface of the catalyst during the reaction.

TEM images of the fresh catalyst and the measured size distribution of the metallic particles are shown in **Figure 4**, where the characteristic microporosity of the carbonaceous support it can be also observed.

The Ni particle size distribution and the average diameter of the Ni particles were calculated with a number >500 particles, which confers enough significant statistical relevance. In

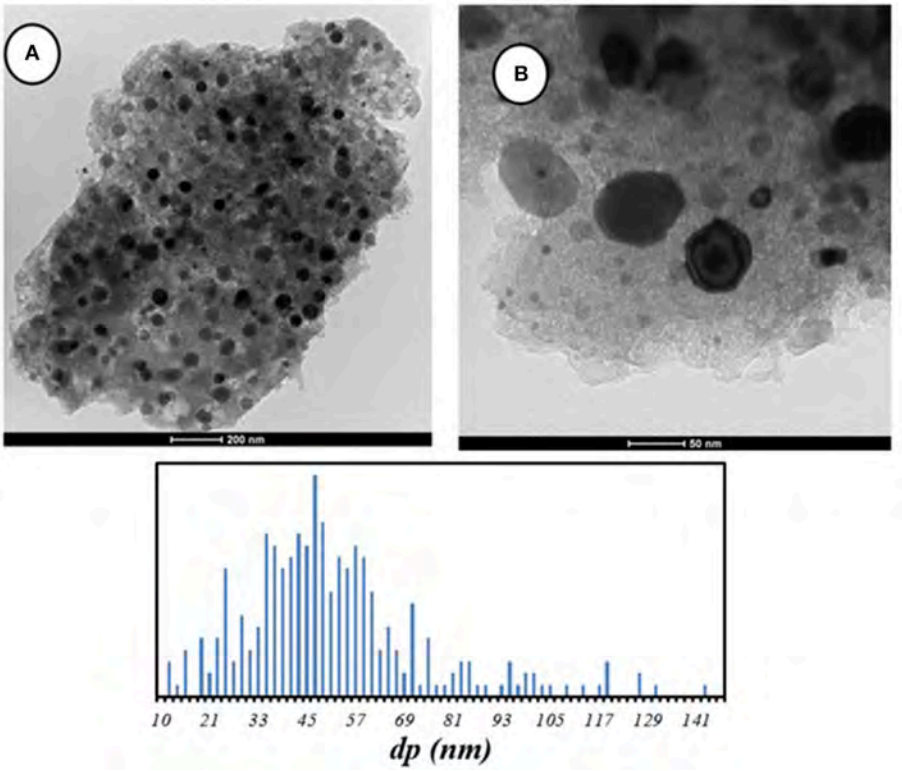

FIGURE 4 | TEM images and Ni particle size distribution of fresh catalyst. **(A)** and **(B)** corresponds to different magnifications of the TEM images.

addition, owing to the shape of the Ni particle size distributions obtained, it was decided to calculate the average diameter of the Ni particles using the following expression (Bergeret et al., 1997; Cazaña et al., 2015): $d_{pm} = \Sigma\ (n_i \cdot d_i^3)/\Sigma(n_i \cdot d_i^2)$. In this equation d_{pm} is the average diameter of Ni particles and n_i the number of particles with d_i diameter. The average size of the particle is around 74 nm. As can be seen in this figure, the distribution of the metallic particles size is quite broad, finding relatively small particles (∼13 nm) and very large particles (>100 nm). As was expected, the high temperature used in the thermal decomposition stage of catalyst preparation, leads to the sintering of Ni particles. Nevertheless, this protocol of catalysts preparation avoids any further sintering of the metallic phase at the harsh conditions of reaction used in the present case.

On the other side, the large discrepancy observed between the values of the average Ni particle from Scherrer equation, i.e., the XRD results in **Figure 3**, and the TEM results can be consequence of the broad and asymmetrical distribution of the particle sizes, because the long tail observe at high diameters distorts the calculations.

Figure 5 shows the Raman spectra obtained for the fresh and used catalyst under different reaction conditions. The spectra corresponding to the fresh catalyst, named as Ni/BC, present the two broad peaks, characteristic for this type of biomorphic support (Cazaña et al., 2015, 2018a,b). The wideness of these peaks at 1,350 cm^{-1} (D band) and 1,590 cm^{-1} (G band), is consequence of different structural contributions of the several types graphitic dominies formed during the thermal decomposition stage (Rhim et al., 2010; Cazaña et al., 2018a). The ratio I_G/I_D of these peaks, related to the type and number of defects (Ferrari and Robertson, 2000), is 0.97.

Kinetic and Characterization Results. Influence of the Reaction Conditions

The productivity, measured as g_C/g_{cat}.min, selectivity and stability of the catalyst during the reaction have been studied as a function of the temperature and methane concentration in the feed.

In this regard, **Figure 6** shows the effect of reaction temperature on the evolution of the carbon concentration (m_c), expressed as g_C/g_{cat}, along the reaction time. The feed composition used for these experiments was 14.3% H_2/14.3% CH_4/71.4% N_2. Similarly, in **Figure 7** is shown the influence of the methane concentration of the feed. The experiments were carried out at 950°C with a 14.3% H_2 in all the cases and balanced concentrations of N_2. The slope of the curves at each point is the reaction rate at that time. The presence of H_2 in the feed maintains part of the surface of the Ni nanoparticles free of amorphous carbon, and, in consequence, the activity of the catalyst is longer. In addition, it has been observed (Cazaña et al., 2018a) that in presence of H_2 the carbon formed during the reaction has fewer defects.

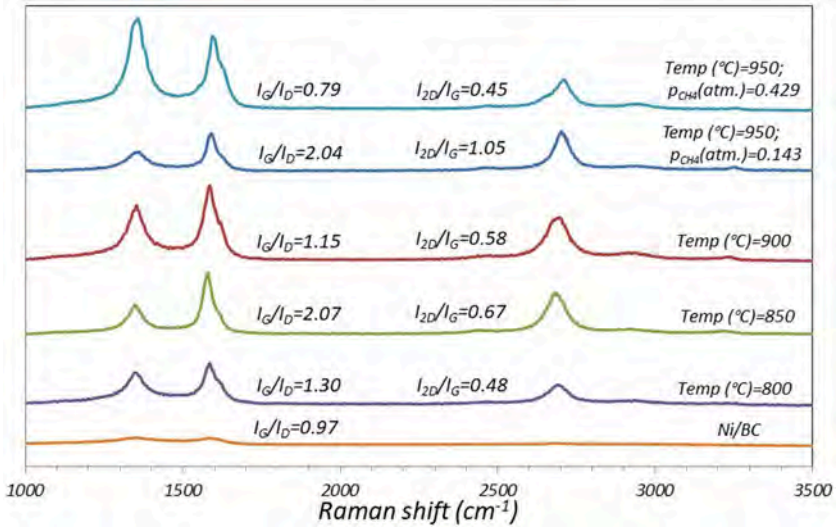

FIGURE 5 | Raman spectra of fresh catalyst and after reaction at different temperatures and with different methane concentrations.

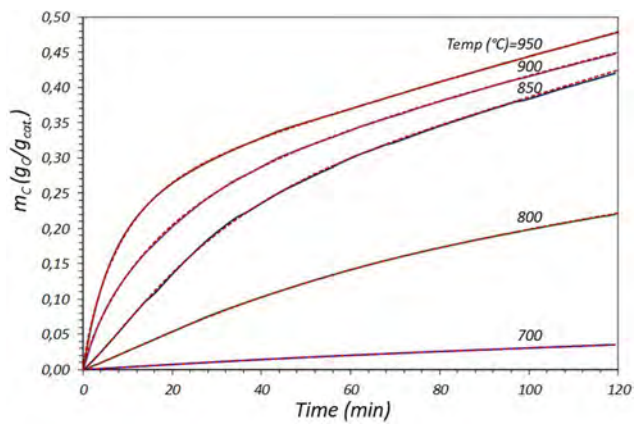

FIGURE 6 | Evolution of carbon content along time. Influence of reaction temperature. Red dotted lines: Model prediction.

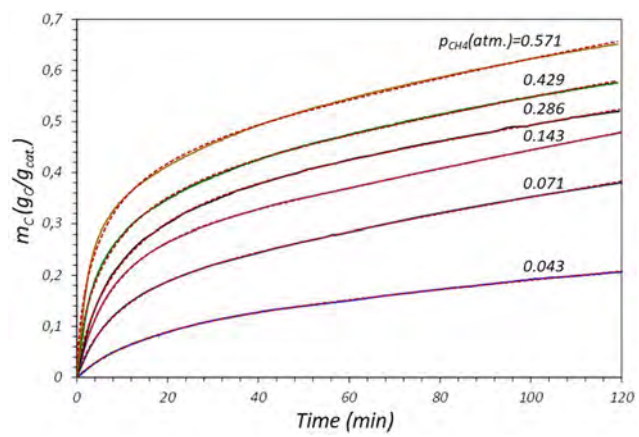

FIGURE 7 | Evolution of carbon content along time. Influence of CH_4 concentration. Red dotted lines: Model prediction.

As regards the influence of the reaction temperature shown in **Figure 8**, the carbon productivity increase monotonically attaining, after 2 h of reaction, a maximum value of 0.24 g_C/g_{cat} h at 950°C, corresponding to a content of 0.48 g_C/g_{cat}. On the contrary, at 700°C the productivity is very low, 0.018 g_C/g_{cat}.h.

The increase in the methane concentration in the feed, see **Figure 7**, also caused a rise in the amount of carbon deposited on the catalyst. Thus, the productivity passes from 0.103 g_C/g_{cat} h at a 4.3% of CH_4 to 0.325 g_C/g_{cat} h at 57.14% of CH_4 in the feed.

The shape of all curves in **Figures 6**, **7** is similar, showing a high initial slope corresponding to a high reaction rate and, gradually, a continuous decrease in the rate, until reaching a final value corresponding to a slow increase in the amount of carbon deposited. The rate attained at the final time of operation is determined by the residual activity of the catalyst, as it is considered by the kinetic model proposed above. It must be noted that all the experiments of the influence of methane concentration have been carried out at high temperature i.e., 950°C.

In the present case, both, the reaction temperature and the methane concentration, have similar effects on the evolution of the carbon concentration along time. Thus, the increase in the temperature and in the partial pressure of CH_4 augments the initial reaction rate and the final amount of carbon deposited on the catalysts.

After the initial period of increasing rate, in all the cases it is observed a decay of the catalyst activity until to attain a residual rate characterized by a low value of the slope of the curves at the end of the reaction time.

In this point, is interesting to note that the XRD results in **Figure 3** do not indicate the additional sintering of the nanoparticles during the reaction, therefore the deactivation

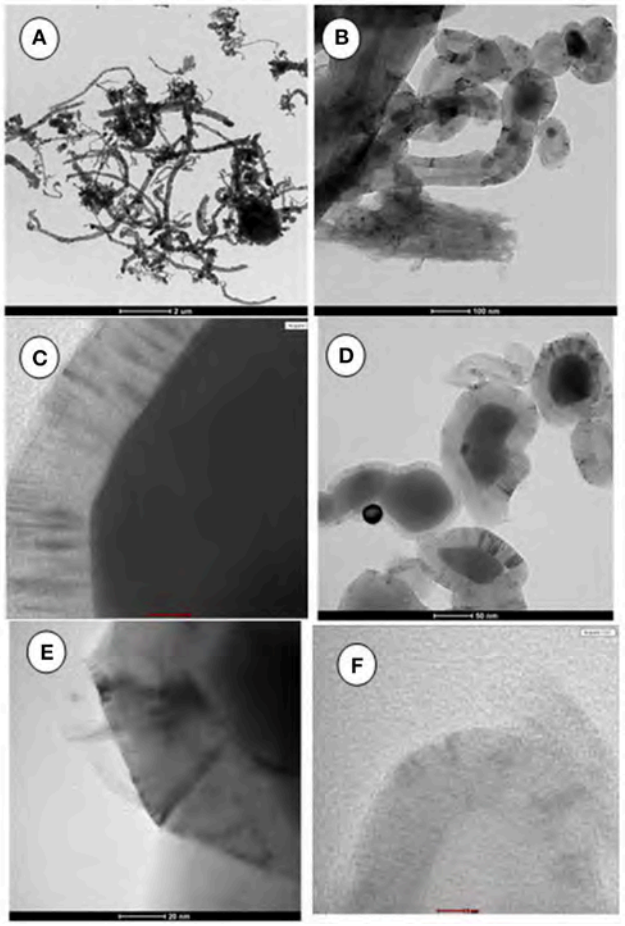

FIGURE 8 | TEM images of Ni/BC catalyst after reaction at: 850°C **(A,B)**: 900°C; **(C,D)** 950°C **(E,F)**.

can be related to the effects of coke deposition (temperatures until 850°C), or to the build-up of the graphitic nanolayers at higher temperatures.

Thus, TEM micrographs presented in **Figure 8** show the formation of carbon nanofibers with bamboo-like structure at 850°C (**Figures 8A,B**). At this temperature, in some cases, it can be also seen the presence of metallic nanoparticles in the inner part of the carbon nanofibers, which have been trapped during the growth of these CNFs.

The wide distribution of Ni nanoparticle sizes (**Figure 4**) leads consequently to a wide distribution of the CNFs diameters, covering a range from 50 to 100 nm approximately. As previously commented, the large and broad distribution of catalyst nanoparticles sizes is related to the high temperature and rate of heating used during the thermal decomposition stage of catalyst synthesis, triggering the sintering of the metallic nanoparticles during their synthesis.

At elevated temperatures of reaction, above 850°C, TEM images (**Figures 8C–F**) do not show the formation of carbon nanofibers. In this case, the carbon formed is in form graphitic nanoplatelets, which are surrounding the metallic nanoparticles. In addition, in some cases the graphite layers are being exfoliated (**Figure 8F**) forming unstructured layers of carbon, which evolve to form graphene and FLG ("few layer graphene") materials (Ferrari et al., 2006; Graf et al., 2007; Faugeras et al., 2008; Geim, 2009).

Figure 5 shows Raman spectra of the catalyst samples after different reaction conditions in addition to the spectra corresponding to the fresh catalyst, Ni/BC. In all the cases are present the three peaks corresponding to the D band (1,350 cm^{-1}), the G band (1,590 cm^{-1}), and the 2D band (2,700 cm^{-1}). Obviously, the formation of carbonaceous nanomaterials during the reaction largely increases the intensity of these band and in the case of the 2D band, this only appears after reaction, indicating the formation of graphitic/graphenic materials (Malard et al., 2009; Ferrari and Basko, 2013). Besides, the separation between the D and G bands is quite clear, and the intermediate peak between both has almost disappeared, indicating a good coverage of the surface of the support with the carbon formed.

For the experiments at 900 and 950 the values of the I_{2D}/I_G and I_G/I_D ratios are ranged from 0.45 to 1.05 and 0.79 to 2.04, respectively, which indicate that the sample contains mostly graphite and FLG materials, in agreement with the results observed in TEM (Takenaka et al., 2003; Zhang et al., 2008). At these temperatures, in particular at 950°C, the increase in the partial pressure of methane in the feed (from 0.143 to 0.429 atm.), causes a notorious decrease in the I_{2D}/I_G and I_G/I_D ratios, indicating that the carbon formed in these conditions contains more defects on their structure. Therefore, although, the amount of carbon formed is higher, see **Figure 6**, their average quality is lower.

In summary, at increasing reaction temperatures and/or methane concentrations, the methane cracking rate increases leaving a higher number of atoms of carbon on the Ni surface, which is quickly carburized. In these conditions, the amount of the carbon atoms dissolved on the metallic subsurface becomes very high, attaining a supersaturation state. Consequently, the driving force for the diffusion of the carbon atoms through the Ni nanoparticles is large, favoring a rapid precipitation of the carbon at the rear surface of the Ni nanoparticles to form carbonaceous nanomaterials (CMNs).

As it has been commented above, both the type of CMN formed, and their rate of growth are consequence of a subtle equilibrium between the rates of nucleation and of segregation-precipitation at the exit points of a metallic nanoparticle. If the nucleation rate is low, it is favored the formation of CNTs and CNFs because, once the precipitation of the carbon atoms begins, rapidly the concentration inside the nanoparticle falls below its solubility level, and a steady grow of CNFs is observed, see TEM pictures in **Figures 8A,B**.

On the contrary, if the rate of nucleation is high, the number of exit points can be very large, and the drainage of the carbon atoms occurs in parallel at all the point of the external surface of the Ni nanoparticles, forming graphenic layers surrounding these nanoparticles. The accumulation of these graphenic layers finally forms the observed graphitic nanoplatelets; see TEM pictures in **Figures 8C–F**. Given that the formation of the graphitic nanoplatelets is observed only

at high temperatures, the activation energy associated to the nucleation process must be higher than the one corresponding to the segregation-precipitation step. Notoriously, in **Figures 8E,F** it can be appreciated that some of the graphitic nanolayers formed are exfoliated during the reaction, resulting in separated layers of graphene.

As it has been considered in the development of the kinetic model, the decrease of the reaction rate is the consequence of the catalyst deactivation. However, given that there is a notorious change on the reaction mechanism with the reaction temperature, see **Figure 8**, the causes of the activity decay is different. Thus, at lower temperatures, below 900°C, are mainly formed CNFs because the rate of precipitation of carbon if higher than the rate of nucleation. In this case, the deactivation can be explained by the fouling of the surface of the Ni nanoparticles by the coke formed after the adsorption and decomposition of the molecules of methane. This coke is formed by oligomerization/polymerization of C_nH_m intermediate species formed during the dehydrogenation of methane molecules over the Ni surface (Rodríguez et al., 1995; Bartholomew, 2001). However, part of this coke can be removed by gasification by the hydrogen formed during the reaction, recovering part of the catalyst activity. This fact is taken into account in the kinetic model by means of the Ψ_r parameter.

At high reaction temperatures, the causes of catalyst decay can be related to the complex phenomena involved during the diffusion of the reactants through the layers of graphite, the reconstruction and encapsulation of the metallic nanoparticles during the reaction, and the steric hindrance to the growth of graphitic nanomaterials in the form of layers (Cazaña et al., 2018b). These considerations are supported by the XRD, TEM, and Raman results shown in **Figures 3**, **5**, **8**.

With respect to the results of the application of the kinetic model to the experimental data, in **Figures 6**, **7** it can be seen that the fitting obtained in all the cases is quite good, attaining very high values of the coefficients of correlation ($R^2 > 0.999$) and of the MSC parameter (MSC > 7.6). The values of the fitting parameters are represented on the **Figures 9**–**11**.

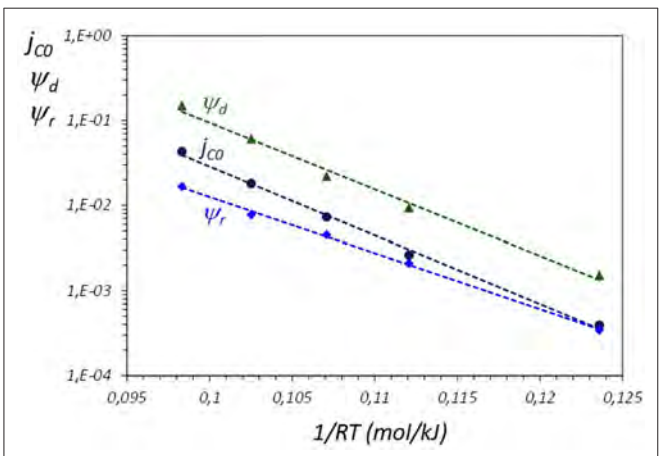

FIGURE 9 | Arrhenius plot of the kinetic parameters. p_{CH4} = 0.1428 atm.

Relating to the effect of the temperature, **Figure 9** contains the Arrhenius plots for the parameters related to the intrinsic rate of carbon growth (j_{C0}), deactivation (Ψ_d), and regeneration (Ψ_r). The values of the apparent activation energies are: E_c = 188.3 kJ/mol, E_d = 180.3 kl/mol, and E_r = 137.1 kJ/mol, respectively. However, analyzing with more detail these data, it can be appreciated that the slope of the high temperature zone takes higher values that in the low temperature zone. This fact can be interpreted as an increase in the activation energies from 143 to 220 kJ/mol for j_{C0} and from 158 to 203 for Ψ_d. These changes are in agreement with the experimental results observed in **Figures 8A–F**. In addition, the activation energy for the parameter Ψ_d is higher than the one corresponding to Ψ_r, therefore, the residual activity of the catalyst, defined in Equation 3, decreases as the temperature rises.

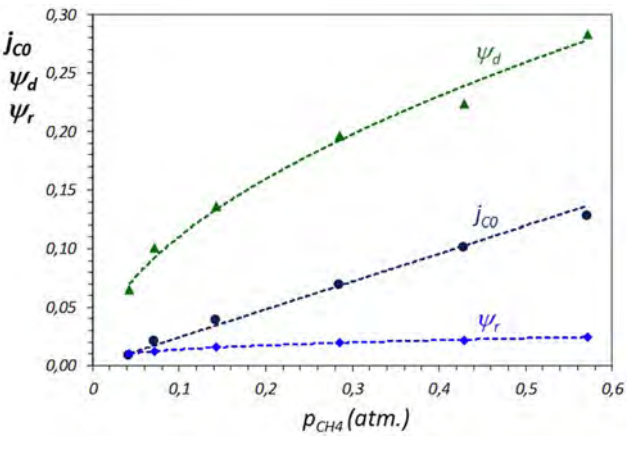

FIGURE 10 | Influence of CH_4 concentration on the kinetic parameters.

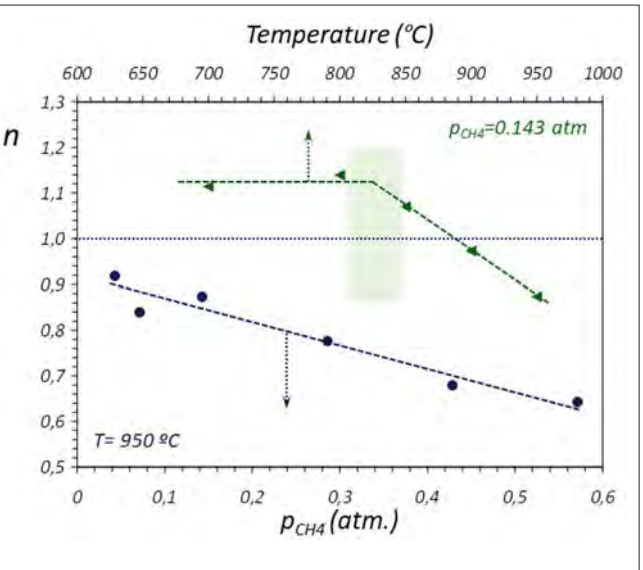

FIGURE 11 | Influence of temperature and methane concentration on the kinetic parameter *n* of Equation 7.

The effect of the p_{CH4}, on the values of the kinetic parameters is shown in **Figure 10**. The application of power-law functions, Equation 8, to these data gives the following values for the kinetic orders: $m_C = 0.90$, $m_d = 0.65$, $m_r = 0.27$. The value of the kinetic order related to the j_{C0} parameter, close to one, is in agreement with the previous results obtained with Ni catalysts for the methane activation reactions (Wei and Iglesia, 2004). On the other side, a value of 0.65, for the kinetic order related to Ψ_d can be explained in terms of a LHHW formalism, as the consequence of strong influence of the methane adsorption during the in the intrinsic stage of deactivation. As expected, the effect of the methane concentration on the Ψ_r parameter is quite low as corresponds to the low value of the kinetic order (0.27). The amount of hydrogen produced in the reaction is low because the conversions attained in the experimental device used are low. However, during the operation at high conversion of methane this point can be very important to modulate the long-term stability of the catalysts.

Finally, in **Figure 11** are presented the values of the parameter n, introduced in the Equation 7. As it has been discussed above, this parameter allows taking into account the effect of the different characteristics diffusion times of carbon in each range of reaction temperature. Thus, at low temperature, the precipitation of the CNFs is the controlling stage and at high temperatures the nucleation-segregation of the graphenic nanoplatelets is what controls. Therefore, the values in **Figure 11** are in agreement with this interpretation. Above 850°C, the value of the parameter n decreases, indicating a change in the controlling step of the carbon segregation (Cazaña et al., 2018a). This change is also observed in the Arrhenius plot, **Figure 9**, for the j_{C0} and Ψ_d parameters.

Accordingly, and given that all the experiments done to analyse the influence p_{CH4}, were carried out at 950°C, all the values obtained for the parameter n were lower than one and n decreases as the methane concentration increase.

CONCLUSIONS

A catalyst of Ni (24%wt.) supported on Biomorphic Carbon residues, has been synthesized using vine shoots residues, which are an important waste in viniculture. The preparation method involves a simple one-step thermal decomposition stage. The main textural properties, BET area of 63 m^2/g and 56% of microporosity, of the catalyst synthesized indicates that these materials are suitable for reactions which participate reagents in gas phase, even in the harsh conditions used during the decomposition of methane.

Thus, the catalyst has proved to be active in the synthesis of carbon nanofibers and graphene related materials by catalytic decomposition of methane at elevated temperatures.

The productivity, type and quality of the carbonaceous nanomaterials obtained are deeply dependent on the operating conditions during the reaction.

The results of this study indicate that nanocarbonaceous material productivity increases with the reaction temperature and the partial pressure of methane because the decomposition rate of methane increases under these operating conditions.

As an important fact, is has been obtained that the reaction temperature strongly affect the type of the nanomaterial produced. Thus, at temperatures until 850°C it is produced CNFs of bamboo type. Above this critical temperature, it is mainly obtained nanolayers of graphitic nature. This fact is a consequence of the change on the balance of diffusion-nucleation-precipitation of the dissolved carbon atoms inside the Ni nanoparticles. At low temperatures the process is governed by the precipitation forming CNFs. At elevated temperatures, the high nucleation rates attained determine the formation of nanolayers surrounding the Ni nanoparticles.

The kinetic model used to analyze the experimental data is based on the effect of each of the main stages of the mechanism of reaction. The values of the parameters have a clear physical meaning and their evolution with the temperature and the methane concentration is in agreement with the model hypothesis.

The characterization results indicate that the highest quality graphenic materials were obtained operating at 950°C with 14.3% of CH_4 and 14.3% of H_2. Under these conditions, the Raman spectra and TEM images have shown that the nanocarbonaceous material consists mainly of few layer graphene and graphitic nanolayers surrounding the Ni nanoparticles. The nanoplatelets, are eventually exfoliated during the reaction resulting in separated layers of graphene.

DATA AVAILABILITY

All datasets generated for this study are included in the manuscript and the supplementary files.

AUTHOR CONTRIBUTIONS

MA, FC, JV, and VS performed the experiments. NL, ER, and AM contributed to the planning, the interpretation of results and the writing of the manuscript.

ACKNOWLEDGMENTS

We acknowledge financial support from MINECO (Madrid, Spain) FEDER, Projects ENE2017-82451-C3 y ENE2013-47880-C3.

REFERENCES

Ahmed, S., Aitani, A., Rahman, F., Al-Dawood, A., and Al-Muhaish, F. (2009). Decomposition of hydrocarbons to hydrogen and carbon. *Appl. Catal. A Gen.* 359, 1–24. doi: 10.1016/j.apcata.2009.02.038

Amin, A. M., Croiset, E., and Epling, W. (2011). Review of methane catalytic cracking for hydrogen production. *Int. J. Hydrogen Energy* 36, 2904–2935. doi: 10.1016/j.ijhydene.2010.11.035

Armenise, S., Garcia-Bordeje, E., Valverde, J. L., Romeo, E., and Monzón, A. (2013). A Langmuir–Hinshelwood approach to the kinetic modelling of catalytic

ammonia decomposition in an integral reactor. *Phys. Chem. Chem. Phys*. 15, 12104–12117. doi: 10.1039/c3cp50715g

Ashik, U. P. M., Daud, W. M. A. W., and Abbas, H. F. (2015). Production of greenhouse gas free hydrogen by thermocatalytic decomposition of methane–A review. *Renew. Sust. Energy Rev*. 44, 221–256. doi: 10.1016/j.rser.2014.12.025

Azuara, M., Sáiz, E., Manso, J. A., García-Ramos, F. J., and Manyà, J. J. (2017). Study on the effects of using a carbon dioxide atmosphere on the properties of vine shoots-derived biochar. *J. Anal. Appl. Pyrol*. 124, 719–725. doi: 10.1016/j.jaap.2016.11.022

Baddour, C. E., and Briens, C. (2005). Carbon nanotube synthesis: a review. *Int. J. Chem. React. Eng*. 3:R3. doi: 10.2202/1542-6580.1279

Bartholomew, C. H. (2001). Mechanisms of catalyst deactivation. *Appl. Catal. A Gen.* 212, 17–60. doi: 10.1016/S0926-860X(00)00843-7

Benito, P., Herrero, M., Labajos, F. M., Rives, V., Royo, C., Latorre, N., et al. (2009). Production of carbon nanotubes from methane: use of Co-Zn-Al catalysts prepared by microwave-assisted synthesis. *Chem. Eng. J*. 149, 455–462. doi: 10.1016/j.cej.2009.02.022

Bergeret, G., Gallezot, P., Ertl, G., Knözinger, H., and Weitkamp, J. (Eds) (1997). *Handbook of Heterogeneous Catalysis*. Vol. 3. Weinheim: Wiley-VCH. 738 p.

Cazaña, F., Galetti, A., Meyer, C., Sebastián, V., Centeno, M. A., Romeo, E., et al. (2018b). Synthesis of Pd-Al/biomorphic carbon catalysts using cellulose as carbon precursor. *Catal. Today* 301, 226–238. doi: 10.1016/j.cattod.2017.05.026

Cazaña, F., Jimaré, M. T., Romeo, E., Sebastián, V., Irusta, S., Latorre, N., et al. (2015). Kinetics of liquid phase cyclohexene hydrogenation on Pd–Al/biomorphic carbon catalysts. *Catal. Today* 249, 127–136. doi: 10.1016/j.cattod.2014.11.022

Cazaña, F., Latorre, N., Tarifa, P., Labarta, J., Romeo, E., and Monzón, A. (2018a). Synthesis of graphenic nanomaterials by decomposition of methane on a Ni-Cu/biomorphic carbon catalyst. Kinetic and characterization results. *Catalysis Today* 299, 67–79. doi: 10.1016/j.cattod.2017.03.056

Chen, D., Christensen, K. O., Ochoa-Fernández, E., Yu, Z., Tøtdal, B., Latorre, N., et al. (2005). Synthesis of carbon nanofibers: effects of Ni crystal size during methane decomposition. *J. Catal*. 229, 82–96. doi: 10.1016/j.jcat.2004.10.017

Cheng, R., Bai, J., Liao, L., Zhou, H., Chen, Y., Liu, L., et al. (2012). High-frequency self-aligned graphene transistors with transferred gate stacks. *Proc. Natl. Acad. Sci. U.S.A*. 109, 11588–11592. doi: 10.1073/pnas.1205696109

Dubinin, M. M., and Radushkevich, L. V. (1947). Equation of the characteristic curve of activated charcoal. *Proc Acad Sci U.S.S.R. Phys Chem. Sect*. 55, 331–333.

Duca, D., Toscano, G., Pizzi, A., Rossini, G., Fabrizi, S., Lucesoli, G., et al. (2016). Evaluation of the characteristics of vineyard pruning residues for energy applications: effect of different copper-based treatments. *J Agric Eng.* 497, 22–27. doi: 10.4081/jae.2016.497

Dussault, L., Dupin, J. C., Guimon, C., Monthioux, M., Latorre, N., Ubieto, T., et al. (2007). Development of Ni–Cu–Mg–Al catalysts for the synthesis of carbon nanofibers by catalytic decomposition of methane. *J. Catal*. 251, 223–232. doi: 10.1016/j.jcat.2007.06.022

El Achaby, M., El Miri, N., Hannache, H., Gmouh, S., Ben, H., and youcef, Aboulkas, A. (2018). Production of cellulose nanocrystals from vine shoots and their use for the development of nanocomposite materials. *Int J Biol Macromol.* 117, 592–600. doi: 10.1016/j.ijbiomac.2018.05.201

Fan, T. X., Chow, S. K., and Zhang, D. (2009). Biomorphic mineralization: from biology to materials. *Prog. Mat. Sci*. 54, 542–659. doi: 10.1016/j.pmatsci.2009.02.001

Faugeras, C., Nerriere, A., Potemski, M., Mahmood, A., Dujardin, E., Berger, C., et al. (2008). Few-layer graphene on SiC, Pyrolitic graphite, and graphene: a raman scattering study. *Appl. Phys. Lett.* 92:011914. doi: 10.1063/1.2828975

Ferrari, A. C., and Basko, D. M. (2013). Raman spectroscopy as a versatile tool for studying the properties of graphene. *Nat. Nanotechnol*. 8, 235–246. doi: 10.1038/nnano.2013.46

Ferrari, A. C., Meyer, J. C., Scardaci, V., Casiraghi, C., Lazzeri, M., Mauri, F., et al. Geim, A.K. (2006). Raman spectrum of graphene and graphene layers. *Phys. Rev. Lett*. 97:187401. doi: 10.1103/PhysRevLett.97.187401

Ferrari, A. C., and Robertson, J. (2000). Interpretation of Raman spectra of disordered and amorphous carbon. *Phys. Rev. B* 61, 14095–14107. doi: 10.1103/PhysRevB.61.14095

Geim, A. K. (2009). Graphene: status and prospects. *Science* 324, 1530–1534. doi: 10.1126/science.1158877

Graf, D., Molitor, F., Ensslin, K., Stampfer, C., Jungen, A., Hierold, C., et al. (2007). Spatially resolved raman spectroscopy of single-and few-layer graphene. *Nano Lett.* 7, 238–242. doi: 10.1021/nl061702a

Hu, N., Yang, Z., Wang, Y., Zhang, L., Wang, Y., Huang, X., et al. (2014). Ultrafast and sensitive room temperature NH_3 gas sensors based on chemically reduced graphene oxide. *Nanotechnology* 25:025502. doi: 10.1088/0957-4484/25/2/025502

Ji, L., Tan, Z., Kuykendall, T. R., Aloni, S., Xun, S., Lin, E., et al. (2011). Fe_3O_4 nanoparticle-integrated graphene sheets for high-performance half and full lithium ion cells. *Phys. Chem. Chem. Phys*. 13, 7170–7177. doi: 10.1039/c1cp20455f

Latorre, N., Cazaña, F., Martínez-Hansen, V., Royo, C., Romeo, E., and Monzón, A. (2011). Ni-Co-Mg-Al catalysts for hydrogen and carbonaceous nanomaterials production by CCVD of methane. *Catal. Today* 172, 143–151. doi: 10.1016/j.cattod.2011.02.038

Latorre, N., Romeo, E., Cazaña, F., Ubieto, T., Royo, C., Villacampa, J. I., et al. (2010a). Carbon nanotube growth by catalytic chemical vapor deposition: a phenomenological kinetic model. *J. Phys. Chem. C* 114, 4773–4782. doi: 10.1021/jp906893m

Latorre, N., Romeo, E., Villacampa, J. I., Cazaña, F., Royo, C., and Monzón, A. (2010b). Kinetics of carbon nanotubes growth on a Ni–Mg–Al catalyst by CCVD of methane: influence of catalyst deactivation. *Catal. Today* 154, 217–223. doi: 10.1016/j.cattod.2010.03.065

Li, Y., Li, D., and Wang, G. (2011). Methane decomposition to COx-free hydrogen and nano-carbon material on group 8–10 base metal catalysts: a review. *Catal. Today* 162, 1–48. doi: 10.1016/j.cattod.2010.12.042

Malard, L. M., Pimenta, M. A., Dresselhaus, G., and Dresselhaus, M. S. (2009). Raman spectroscopy in graphene. *Phys. Rep*. 473, 51–87. doi: 10.1016/j.physrep.2009.02.003

Mann, S. (2001). *Biomineralization: Principles and Concepts in Bioinorganic Materials Chemistry*. Oxford: Oxford University Press.

Manyà, J. J., González, B., Azuara, M., and Arner, G. (2018). Ultra-microporous adsorbents prepared from vine shoots-derived biochar with high CO_2 uptake and CO_2/N_2 selectivity. *Chem. Eng. J*. 345, 631–639. doi: 10.1016/j.cej.2018.01.092

Martínez-Hansen, V., Latorre, N., Royo, C., Romeo, E., García-Bordejé, E., and Monzón, A. (2009). Development of aligned carbon nanotubes layers over stainless steel mesh monoliths. *Catal. Today* 147S, S71–S75. doi: 10.1016/j.cattod.2009.07.010

Monzón, A., Lolli, G., Cosma, S., Mohamed, S. B., and Resasco, D. E. (2008). Kinetic modeling of the SWNT growth by CO disproportionation on CoMo catalysts. *J. Nanosci. Nanotechnol*. 8, 6141–6152. doi: 10.1166/jnn.2008.SW21

Monzón, A., Romeo, E., and Borgna, A. (2003). Relationship between the kinetic parameters of different catalyst deactivation models. *Chem. Eng. J*. 94, 19–28. doi: 10.1016/S1385-8947(03)00002-0

Nine, M. J., Cole, M. A., Tran, D. N. H., and Losic, D. (2015). Graphene: a multipurpose material for protective coatings. *J. Mater. Chem. A* 3, 12580–12602. doi: 10.1039/C5TA01010A

Novoselov, K. S. (2011). Nobel lecture: graphene: materials in the flatland. *Rev. Mod. Phys*. 83, 837–849. doi: 10.1103/RevModPhys.83.837

Pérez-Cabero, M., Romeo, E., Royo, C., Monzón, A., Guerrero-Ruíz, A., and Rodríguez-Ramos, I. (2004). Growing mechanism of CNTs: a kinetic approach. *J. Catal*. 224, 197–205. doi: 10.1016/j.jcat.2004.03.003

Rhim, Y.-R., Zhang, D., Fairbrother, D. H., Wepasnick, K. A., Livi, K. J., Bodnar, R. J., et al. (2010). Changes in electrical and microstructural properties of microcrystalline cellulose as function of carbonization temperature. *Carbon* 48, 1012–1024. doi: 10.1016/j.carbon.2009.11.020

Rodríguez, J. C., Peña, J. A., Monzón, A., Hughes, R., and Li, K. (1995). Kinetic modelling of the deactivation of a commercial silica-alumina catalyst during isopropylbenzene cracking. *Chem. Eng. J*. 58, 7–13. doi: 10.1016/0923-0467(94)02879-F

Romeo, E., Saeys, M., Monzón, A., and Borgna, A. (2014). Carbon nanotube formation during propane decomposition on boron-modified Co/Al_2O_3 catalysts: a kinetic study. *Int. J. Hydrogen Energy* 39, 18016–18026. doi: 10.1016/j.ijhydene.2014.04.168

Sclove, S. (1987). Application of model-selection criteria to some problems in multivariate analysis. *Psychometrika* 52, 333–343.

Serrano, D. P., Botasa, J. A., Pizarro, P., and Gómeza, G. (2013). Kinetic and autocatalytic effects during the hydrogen production by methane decomposition over carbonaceous catalysts. *Int. J. Hydrogen Energy* 38, 5671–5683. doi: 10.1016/j.ijhydene.2013.02.112

Shin, J., and Kim, J. T. (2015). Broadband silicon optical modulator using a graphene-integrated hybrid plasmonic waveguide. *Nanotechnology* 26:365201. doi: 10.1088/0957-4484/26/36/365201

Siamaki, A. R., Khder, A. E. R. S., Abdelsayed, V., El-Shall, M. S., and Gupton, B. F. (2011). Microwave-assisted synthesis of palladium nanoparticles supported on graphene: a highly active and recyclable catalyst for carbon–carbon cross-coupling reactions. *J. Catal.* 279, 1–11. doi: 10.1016/j.jcat.2010.12.003

Suelves, I., Pinilla,. J. L., Lázaro, M. J., and Moliner, R. (2008). Carbonaceous materials as catalysts for decomposition of methane. *Chem. Eng. J.* 140, 432–438. doi: 10.1016/j.cej.2007.11.014

Takenaka, S., Kobayashi, S., Ogihara, H., and Otsuka, K. (2003). Ni/SiO_2 catalyst effective for methane decomposition into hydrogen and carbon nanofiber. *J. Catal.* 217, 79–87. doi: 10.1016/S0021-9517(02)00185-9

Villacampa, J. I., Royo, C., Romeo, E., Montoya, J. A., Del Angel, P., and Monzón, A. (2003). Catalytic decomposition of methane over $Ni\text{-}Al_2O_3$ coprecipitated catalysts: Reaction and regeneration studies. *Appl. Catal. A* 252, 363–383. doi: 10.1016/S0926-860X(03)00492-7

Ward, E. J. (2008). A review and comparison of four commonly used Bayesian and maximum likelihood model selection tools. *Ecol. Model.* 211, 1–250. doi: 10.1016/j.ecolmodel.2007.10.030

Wei, J., and Iglesia, E. (2004), Isotopic and kinetic assessment of the mechanism of reactions of CH4 with CO2 or H2O to form synthesis gas and carbon on nickel catalysts, *J. Catal.*, 224, 370–383. doi: 10.1016/j.jcat.2004.02.032

Will, J., Zollfrank, C., Kaindl, A., Sieber, H., and Greil, P. (2010). Biomorphic ceramics: technologies based on nature. *Keram Z.* 62, 114–120. Available online at: https://www.tib.eu/en/search/id/tema%3ATEMA20100500570/Biomorphe-Keramik-Technologie-nach-dem-Vorbild/#documentinfo

Zhang, G., Sun, S., Yang, D., Dodelet, J. P., and Sacher, E. (2008). The surface analytical characterization of carbon fibers functionalized by H_2SO_4/HNO_3 treatment. *Carbon* 46, 196–205. doi: 10.1016/j.carbon.2007.11.002

Zhang, J., Li, X., Xie, W., Hao, Q., Chen, H., and Ma, X. (2018). Handy synthesis of robust Ni/carbon catalysts for methane decomposition by selective gasification of pine sawdust. *Int. J. Hydrogen Energy* 43, 19414 −19419. doi: 10.1016/j.ijhydene.2018.08.207

Conflict of Interest Statement: The authors declare that the research was conducted in the absence of any commercial or financial relationships that could be construed as a potential conflict of interest.